

Article

# Rational Design of Fullerene Derivatives for Improved Stability of p-i-n Perovskite Solar Cells

Victoria V. Ozerova <sup>1</sup>, Alexander V. Mumyatov <sup>1</sup>, Andrey E. Goryachev <sup>2</sup>, Ekaterina A. Khakina <sup>3,4</sup>, Alexander S. Peregodov <sup>3</sup>, Sergey M. Aldoshin <sup>1</sup> and Pavel A. Troshin <sup>1,\*</sup>

- <sup>1</sup> Federal Research Center for Problems of Chemical Physics and Medicinal Chemistry, Russian Academy of Sciences, Academician Semenov Avenue 1, 142432 Chernogolovka, Russia
- <sup>2</sup> Physics Department, Ariel University, Ramat HaGolan St. 65, Ari'el 40700, Israel
- <sup>3</sup> A. N. Nesmeyanov Institute of Organoelement Compounds of Russian Academy of Sciences, Vavilova St. 28, 119334 Moscow, Russia
- <sup>4</sup> Faculty of Chemistry, National Research University Higher School of Economics, Vavilova St. 7, 101000 Moscow, Russia
- \* Correspondence: troshin2003@inbox.ru

**Abstract:** Perovskite solar cells (PSCs) with p-i-n architecture attracted particular attention from the research community due to their simple and scalable fabrication at low temperatures. However, the operational stability of p-i-n PSCs has to be improved, which requires the development of advanced charge transport interlayers. Fullerene derivatives such as phenyl-C<sub>61</sub>-butyric acid methyl ester (PC<sub>61</sub>BM) are commonly used as electron transport layer (ETL) materials in PSCs, though they strongly compromise the device stability. Indeed, it has been shown that PC<sub>61</sub>BM films actively absorb volatile products resulting from photodegradation of lead halide perovskites and transport them towards top metal electrode. Thus, there is an urgent need for development of new fullerene-based electron transport materials with improved properties, in particular the ability to heal defects on the perovskite films surface and block the diffusion of volatile perovskite photodegradation products. To address this challenge, a systematic variation of organic addends structure should be performed in order to tailor the properties of fullerene derivatives. Herein, we rationally designed a series of fullerene derivatives with different side chains and explored their performance as ETL materials in perovskite solar cells. It has been shown that among all studied compounds, a methanofullerene with thiophene pendant group enables both high efficiency and improved device operational stability. The obtained results suggest that further engineering of fullerene-based materials could pave a way for the development of advanced ETL materials enabling long lifetimes of p-i-n perovskite solar cells.

**Keywords:** fullerene derivatives; methanofullerenes; perovskite solar cells; electron transport materials; ETLs



**Citation:** Ozerova, V.V.; Mumyatov, A.V.; Goryachev, A.E.; Khakina, E.A.; Peregodov, A.S.; Aldoshin, S.M.; Troshin, P.A. Rational Design of Fullerene Derivatives for Improved Stability of p-i-n Perovskite Solar Cells. *Inorganics* **2023**, *11*, 153. <https://doi.org/10.3390/inorganics11040153>

Academic Editors: Zdeněk Slanina, Kyriakos Porfyrakis and Nikos Tagmatarchis

Received: 20 February 2023

Revised: 19 March 2023

Accepted: 28 March 2023

Published: 1 April 2023



**Copyright:** © 2023 by the authors. Licensee MDPI, Basel, Switzerland. This article is an open access article distributed under the terms and conditions of the Creative Commons Attribution (CC BY) license (<https://creativecommons.org/licenses/by/4.0/>).

## 1. Introduction

Perovskite solar cells represent an exceptionally promising emerging photovoltaic technology, which surpassed 25% efficiency threshold and currently struggles with the stability issues [1]. Indeed, complex lead halides used as absorber materials are very sensitive to light and elevated temperatures, as well as to the presence of ambient species such as oxygen and moisture [2,3]. There is growing evidence that the stability of lead halide perovskite films could be dramatically improved through the rational engineering of the adjacent charge transport interlayers [4]. In particular, hole-transport layer (HTL) and ETL both must be highly uniform and impermeable for perovskite aging products to block their diffusion towards the electrodes and further into the surrounding environment. Unfortunately, some conventional fullerene-based materials such as PC<sub>61</sub>BM do not form compact enough films and were shown to be able to absorb and accumulate perovskite aging products such as methylamine, iodomethane, molecular iodine and hydrogen iodide [5].

Diffusion of these species to the top electrode causes its corrosion and device failure, except some specific corrosion-resistant electrode materials are used [6,7]. To mitigate this problem, some new fullerene derivatives have to be designed with much superior isolation characteristics. To address this challenge, the organic addends attached to the cage have to be chosen wisely to enable (1) defect healing at the interface with the perovskite absorber layer and (2) effecting filling of the cavities between bulky fullerene spheroids to block absorption and diffusion of the perovskite aging products [8]. A considerable research effort has been invested to the synthesis and screening new fullerene-based materials, which resulted in a substantial progress in this research area [9–14]. Still, the aforementioned problem of low operational stability of p-i-n perovskite solar cells with the fullerene-based ETLs is not completely solved [15,16]. Among different types of the explored fullerene derivatives, it is worthy to mention methanofullerenes [17–20], pyrrolidinofullerenes [21,22], oxazolofullerenes [23], cyclopentanofullerenes [24] and indene adducts of fullerenes [25] with different pendant units. Increasing attention is paid to the blends of different types of fullerene derivatives [26–28] or fullerene-MXene composites [29], fullerene-perylendiimide dyads and dendrofullerenes [30,31]. Using fluorine-containing fullerene derivatives, which enable moisture-repelling properties of ETL, was considered as a promising approach for extending ambient stability of p-i-n PSCs [32–34].

Herein, we present the synthesis, characterization and systematic study of a series of methanofullerenes **F1–F8** as electron transport layer materials in PSCs (Figure 1). Differently functionalized methanofullerenes were used since they are related to PC<sub>61</sub>BM, the most commonly used electron transport material for p-i-n PSCs. The choice of structures of the target compounds was rationalized as follows. Compound **F1** represents a longer-chain analogue of ThC<sub>61</sub>BM material reported previously [35]. The thiophene ring is expected to be capable of defect healing on the surface of lead halide perovskite films particularly due to the chelation of undercoordinated Pb<sup>2+</sup> surface cations by sulfur atom. Increase in the length of aliphatic substituent in **F1** was expected to increase material solubility in organic solvents and thus improve the film's quality. The heptyl ester groups were introduced in compounds **F2–F3** for the same purpose. Compound **F4** was loaded with a fluorinated side chain considering the advantages of such type of compounds as discussed above. Compounds **F5–F7** were engineered to enable through-space electronic interactions of the ether oxygen atoms with the fullerene  $\pi$ -system, which were reported to reduce electron affinity of the material (increase LUMO energy) and provide better matching to the perovskite conduction band [36,37]. Finally, compound **F8** was designed through incorporation of a single compact oligoether substituent at the cyclopropane ring to enable (1) high material solubility in organic solvents and (2) good adhesion (due to similar surface energy) of the fullerene derivative to the perovskite absorber layer.

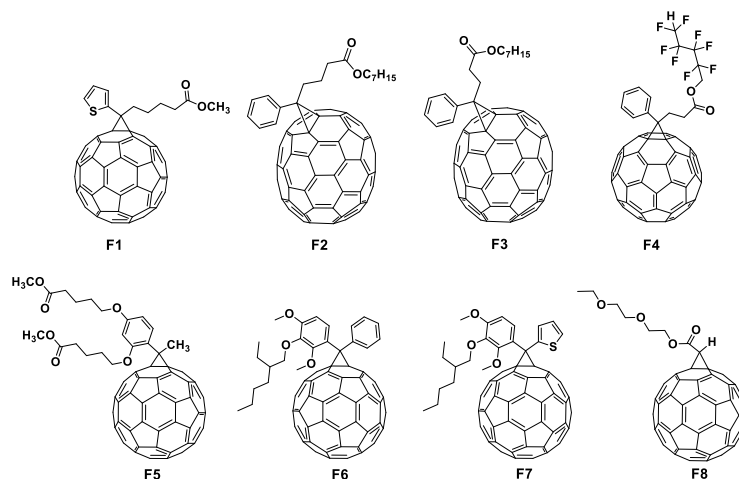
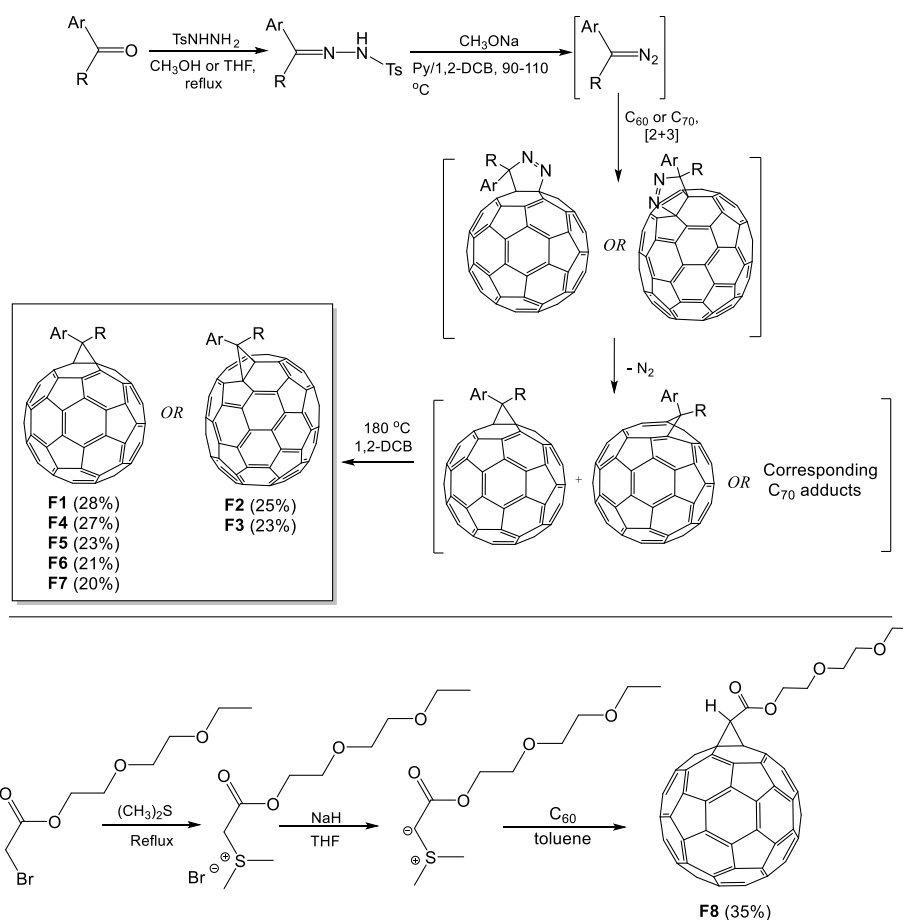


**Figure 1.** Molecular structures of the studied fullerene derivatives. Note: only the structure of the major isomer is shown in the case of [70]fullerene derivatives **F2** and **F3**.

## 2. Results

The synthesis of fullerene derivatives **F1–F8** was accomplished using well-established synthetic methods (Scheme 1) [38,39]. Aromatic ketones were converted to the corresponding tosyl hydrazones by the treatment with tosyl hydrazide in methanol or THF (in the case of **F4** due to lability of the fluoroalkyl ester group). The prepared tosyl hydrazones were used to generate the corresponding diazo compounds in situ upon the treatment with MeONa and pyridine. The [2+3]cycloaddition of diazo compounds to the fullerene cage in 1,2-dichlorobenzene was coupled with the nitrogen extrusion from the intermediate pyrazolinofullerenes, thus affording a mixture of methanofullerenes and fulleroids with an opened 6-5 bond. Heating these mixtures at reflux in 1,2-dichlorobenzene promoted isomerization of the fulleroids to the corresponding methanofullerenes, which were then isolated by column chromatography on silica.



**Scheme 1.** Synthesis of fullerene derivatives **F1–F8**. Notes: (1) product yields given in round brackets are calculated based on the amount of fullerene introduced in the reaction; (2) only the structure of the major isomer is shown in the case of [70]fullerene derivatives **F2** and **F3**.

Compound **F8** was synthesized in a different way starting from the corresponding ester of bromoacetic acid, which was converted to the sulfonium salt in the reaction with dimethyl sulfide. The resulting salt was treated with sodium hydride in THF yielding the corresponding sulfonium ylide, which smoothly undergoes nucleophilic addition to the fullerene cage forming methanofullerene **F8**, which was also isolated by column chromatography on silica.

The purity of all synthesized fullerene derivative was reconfirmed by high-performance liquid chromatography (HPLC); their molecular compositions and structures were supported by mass spectrometry and NMR spectroscopy (see Figures S1–S18 in Supplementary Materials). It should be noted that  $C_{70}$  derivatives **F2** and **F3** were both isolated as mixtures of three regio-

and stereoisomers, which were not resolved even by HPLC (Figure S1). This result is consistent with the previous report on the synthesis and characterization of phenyl- $C_{71}$ -butyric acid methyl ester known as PC<sub>71</sub>BM and other  $C_{70}$  monoaddition products [40,41]. The structures of the major isomers produced by the addition of the organic addends across the [8,25] double bond (IUPAC numbering scheme following [42]) are shown in Figure 1. Two minor isomers were formed via addition across [9,10] double bond and are distinguished by the orientation of unsymmetric organic addend with respect to the fullerene cage (i.e., phenyl group up or phenyl group down). Interestingly, these two minor [9,10] stereoisomers were formed in the amount of ca. 9% each in the case of **F2** (see <sup>1</sup>H NMR in Figure S5), whereas in the case of **F3** their amount was considerably reduced to <4% (Figure S7).

It is worthy to note that compounds **F6** and **F7** showed restricted rotation of bulky substituents at the cyclopropane ring, which resulted in the loss of symmetry plane ( $C_1$  point group symmetry of molecules) and splitting of some signals of organic addends in the <sup>1</sup>H and <sup>13</sup>C NMR spectra suggesting co-existence of at least two atropoisomers.

All synthesized fullerene derivatives showed sufficiently high solubility in organic solvents, in particular, in chlorobenzene (>25–30 mg mL<sup>-1</sup>), to prepare high quality thin films of these compounds required for their evaluation as electron transport materials in p-i-n perovskite solar cells. To probe the influence of the fullerene derivatives **F1–F8** on the optoelectronic properties of the perovskite absorber, we measured photoluminescence (PL) spectra of the MAPbI<sub>3</sub> (MA—methylammonium) thin films prior and after deposition of the upper electron transport layer. It was found that the deposition of PC<sub>61</sub>BM slightly quenches the perovskite PL, whereas depositing compound **F3** has no detectable effect on the emission properties of MAPbI<sub>3</sub> films (Figure S19, SI). A significant decrease in PL intensity was observed for perovskite films, which were coated with the layers of fullerene derivative **F5**, thus suggesting the formation of traps for mobile charge carriers at the perovskite/ETL interface. Fullerene derivatives **F1**, **F2**, **F4**, and **F6–F8** slightly increase the perovskite photoluminescence, which could be explained by healing of the traps, e.g., undercoordinated Pb<sup>2+</sup> cations, which were facilitating non-radiative hole-electron recombination. It was rationalized recently that ETL materials inducing the highest PL intensity of the perovskite absorber layer also deliver the best photovoltaic performance [43]. Thus, the obtained results suggest that the latter group of materials could be more promising for photovoltaic applications.

We also investigated the perovskite/ETL bilayer stacks using infrared scattering near-field optical microscopy (IR s-SNOM), which is a powerful technique enabling spectral mapping of the samples at the characteristic IR frequencies of the individual components. In the case of an ideally defectless MAPbI<sub>3</sub>/ETL stack, mapping at the ETL (fullerene derivative) vibrational frequency should result in a high-intensity signal homogeneously spanning across entire scan area without detectable voids or pinholes. On the contrary, scan at the perovskite frequency (e.g., characteristic for FA cations) should deliver nearly zero intensity without “hot spots”, where perovskite underlayer becomes detectable for IR s-SNOM due to the presence of some defects in the upper layer of the fullerene ETL. For the purpose of the measurement, the selected IR bands of the fullerene ETL material and perovskite absorber should not overlap, even partially. Therefore, we selected different frequencies for perovskite absorber in some case to avoid overlapping with the ETL material.

Figure 2 features some representative sets of IR s-SNOM data obtained for different perovskite/ETL stacks, whereas a complete overview is given in Figure S20 in SI. Thus, almost an ideal behavior was observed for perovskite/**F3** stacks, which show highly uniform perovskite coverage with the fullerene derivative **F3** (uniform red color at the image shown in the center) and no detectable voids or pinholes (absence of red “hot spots” at the image shown on the right side). The perovskite/PC<sub>61</sub>BM stacks revealed multiple point defects (red color on the right image), whose density was considerably reduced in the case of perovskite/**F1** stacks. The most defect structure was observed for perovskite/**F6** stacks: there are noticeable inhomogeneities in the distribution of the fullerene derivative with big pinholes exposing the perovskite absorber on the surface. It seems that high solubility of **F3** promoted the formation

of very uniform films, whereas low solubility of **F6** causes severe inhomogeneities in the film structure. Thus, solubility of fullerene derivatives appears to be an important parameter affecting their performance as ETL materials for perovskite solar cells.

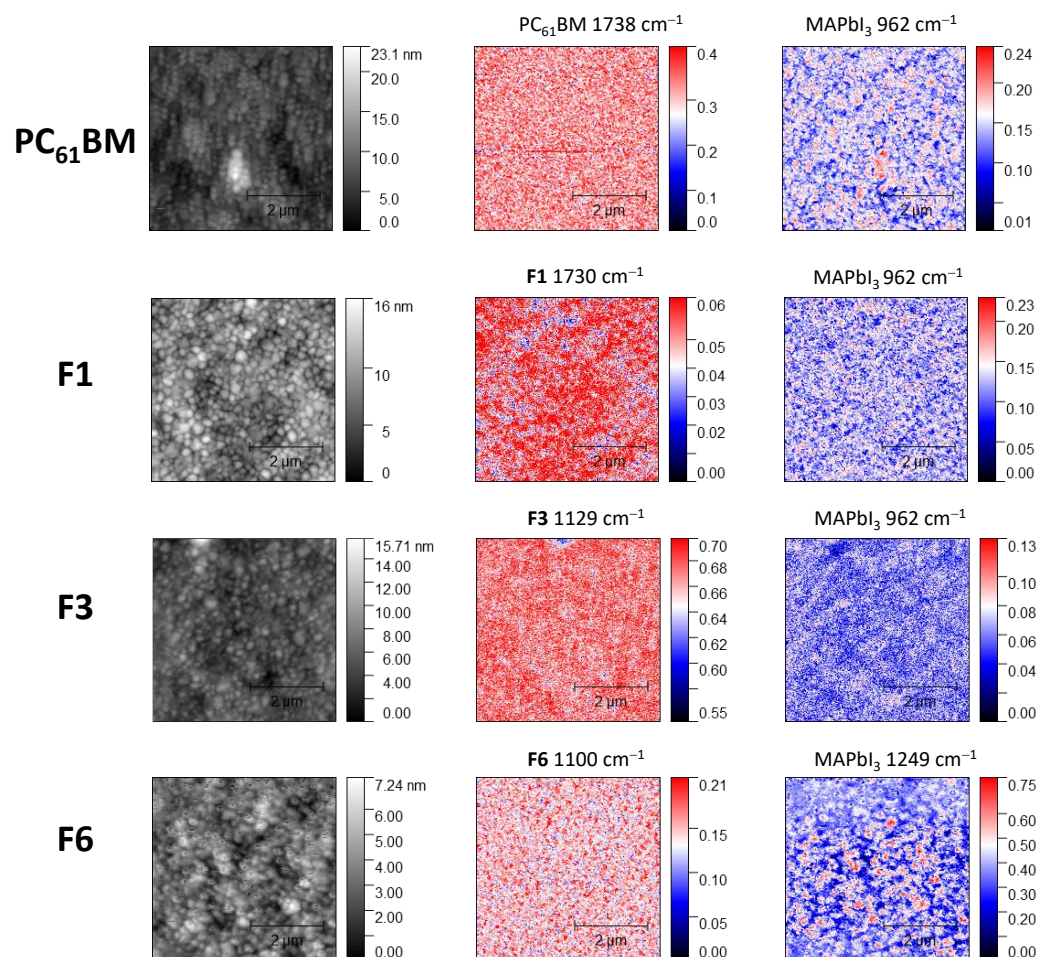


**Figure 2.** Some typical cases of perovskite/ETL bilayer stack morphology: topography (**left column**) and IR s-SNOM images recorded at the characteristic frequencies of the ETL material (**middle column**) and perovskite absorber (**right column**). The used fullerene derivatives are listed on the left side.

All fullerene derivatives were explored as ETL materials in p-i-n PSCs; the device architecture is shown schematically in Figure 3a. To assemble the devices, glass slides covered with transparent conductive layer of tin-doped indium oxide (ITO) were vigorously cleaned and then covered with thin films (~20 nm) of hole transport material poly[bis(4-phenyl)(2,4,6-trimethylphenyl)amine] (PTAA, Figure 3b). Bication cesium-formamidinium ( $\text{Cs}_{0.12}\text{FA}_{0.88}\text{PbI}_3$ ) lead halide perovskite absorber layer was spin coated atop dried PTAA films and subjected to thermal annealing inside the glove box (see details in Materials and Methods). Afterwards, the electron transparent layer was formed by spin-coating chlorobenzene solutions of  $\text{PC}_{61}\text{BM}$  or one of the fullerene derivatives **F1–F8**. The device structure was completed by thermal evaporation of the top metal electrode (Mg/Ag or Al).

The fabricated solar cells were characterized by current–voltage (*J*-*V*) measurements with voltage sweep in forward (F) and reverse (R) directions to obtain open circuit voltage ( $V_{\text{OC}}$ ), short circuit current density ( $J_{\text{SC}}$ ), fill factor (FF) and power conversion efficiency (PCE) values. The hysteresis in the *J*-*V* characteristics was quite small, therefore we present only the curves recorded with reverse voltage sweep in Figure 3c. The photovoltaic parameters extracted from the *J*-*V* characteristics recorded in both directions are presented in Table 1 for champion cells together with average values and standard deviations given

in round brackets. The current densities obtained from  $J$ - $V$  measurements were also reconfirmed by external quantum efficiency (EQE) spectra of the cells integrated against standard solar AM1.5G emission spectrum (Figure 3d).

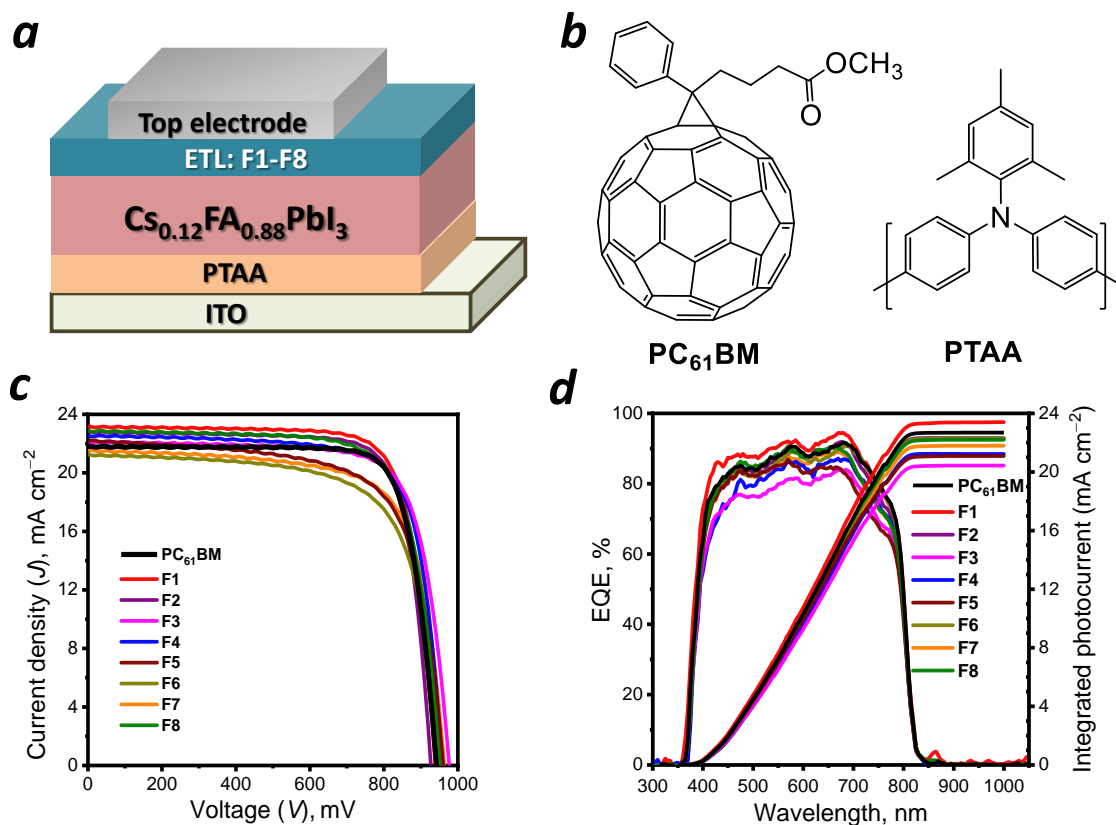


**Figure 3.** Schematic layout of p-i-n perovskite solar cell (a), molecular structures of the standard materials (b), reverse scan current voltage characteristics (c) and EQE spectra (d) of the best devices fabricated using fullerene derivatives F1–F8 as ETL materials.

**Table 1.** Characteristics of perovskite solar cells assembled using different fullerene derivatives as ETL materials \*.

ETL	ETL Concentration and Deposition Rate	Scan Direction	$V_{OC}$ , mV	$J_{SC}$ , $\text{mA cm}^{-2}$	FF, %	PCE, %
$\text{PC}_{61}\text{BM}$	30 $\text{mg mL}^{-1}$ , 3000 rpm	F	936 (947 ± 16)	21.8 (22.1 ± 0.9)	78.5 (74.5 ± 3.4)	16.0 (15.6 ± 0.4)
		R	942 (957 ± 14)	21.8 (22.1 ± 0.9)	79.4 (75.7 ± 2.9)	16.3 (16.0 ± 0.3)
F1	20.2 $\text{mg mL}^{-1}$ , 1500 rpm	F	930 (930 ± 12)	23.0 (22.6 ± 0.4)	77.6 (76.6 ± 1.0)	16.6 (16.1 ± 0.3)
		R	939 (942 ± 7)	23.2 (22.6 ± 0.4)	77.8 (77.4 ± 1.0)	16.9 (16.5 ± 0.2)
F2	16.2 $\text{mg mL}^{-1}$ , 1500 rpm	F	900 (906 ± 18)	22.6 (22.2 ± 0.7)	76.2 (75.6 ± 1.2)	15.5 (15.2 ± 0.3)
		R	927 (929 ± 10)	22.8 (22.2 ± 0.8)	78.2 (78.0 ± 1.3)	16.5 (16.1 ± 0.6)
F3	30 $\text{mg mL}^{-1}$ , 3000 rpm	F	922 (947 ± 15)	23.1 (22.2 ± 0.5)	72.8 (70.6 ± 2.0)	15.5 (14.8 ± 0.5)
		R	977 (967 ± 9)	22.1 (22.2 ± 0.4)	75.9 (73.0 ± 2.2)	16.4 (15.7 ± 0.6)

Table 1. Cont.

ETL	ETL Concentration and Deposition Rate	Scan Direction	$V_{OC}$ , mV	$J_{SC}$ , mA cm <sup>-2</sup>	FF, %	PCE, %
F4	30 mg mL <sup>-1</sup> , 3000 rpm	F	942 (949 ± 11)	22.5 (22.2 ± 0.3)	75.5 (73.9 ± 1.7)	16.0 (15.6 ± 0.6)
		R	958 (962 ± 8)	22.6 (22.2 ± 0.2)	75.7 (73.9 ± 1.6)	16.4 (15.8 ± 0.5)
F5	17.2 mg mL <sup>-1</sup> , 1500 rpm	F	952 (940 ± 28)	22.0 (21.4 ± 0.6)	66.1 (62.2 ± 4.9)	13.8 (12.5 ± 1.3)
		R	961 (954 ± 30)	22.2 (21.4 ± 0.6)	69.5 (67.4 ± 2.5)	14.8 (13.7 ± 1.0)
F6	30 mg mL <sup>-1</sup> , 3000 rpm	F	953 (947 ± 7)	21.2 (20.0 ± 0.9)	67.4 (59.3 ± 4.3)	13.6 (11.3 ± 1.2)
		R	957 (953 ± 5)	21.2 (20.1 ± 0.8)	69.1 (61.7 ± 4.5)	14.0 (11.8 ± 1.3)
F7	30 mg mL <sup>-1</sup> , 3000 rpm	F	954 (955 ± 6)	21.2 (21.3 ± 0.2)	72.9 (70.3 ± 1.7)	14.7 (14.3 ± 0.3)
		R	963 (964 ± 4)	21.5 (21.4 ± 0.2)	72.0 (70.2 ± 1.4)	14.9 (14.5 ± 0.3)
F8	18.8 mg mL <sup>-1</sup> , 2000 rpm	F	950 (937 ± 21)	22.4 (22.3 ± 0.2)	74.1 (71.8 ± 2.9)	15.8 (15.0 ± 0.8)
		R	972 (958 ± 17)	22.5 (22.4 ± 0.3)	74.6 (74.2 ± 0.8)	16.3 (15.9 ± 0.4)

\*—Characteristics obtained from *J-V* curves measured in forward (F) and reverse (R) scan directions with the rate of 10 mV s<sup>-1</sup>. Average parameters and standard deviations given in round brackets were calculated for batches of at least 16 cells. The optimal concentrations of the fullerene derivatives and deposition frequency are given in the second column.

It should be noted that the thickness of the ETL films based on the fullerene derivatives strongly affected the device performance. To find an optimal ETL thickness, we varied concentrations of the fullerene derivatives in their solutions in chlorobenzene and the spin coating frequencies. A typical evolution of the device parameters upon the deposition conditions of the fullerene derivative **F1** is illustrated in Figure S21, Supplementary Materials. One could see that the optimal deposition frequency for the fullerene derivative **F1** was 1500 rpm since it enables the highest device efficiency in combination with the best reproducibility of all photovoltaic parameters. Deposition of this material at higher frequencies leads to some scattering of the device parameters, which could be explained by formation of pinholes in very thin ETL films. On the contrary, going to higher solution concentrations and/or lower deposition frequencies results in too thick ETL films leading to decreased fill factors and PCE values of PSCs. Similar optimization was performed for all studied fullerene derivatives and the optimal ETL processing conditions are given in Table 1.

Considering the data presented in Table 1, one could notice that the best characteristics are delivered by the solar cells using **F1** as ETL material: they clearly outperformed the reference devices assembled using PC<sub>61</sub>BM as ETL. Fullerene derivatives **F4** and **F8** delivered comparable characteristics to PC<sub>61</sub>BM, while other materials showed somewhat inferior photovoltaic performance. Thus, we could conclude that the presence of thiophene ring in **F1** and oligoether chain in **F8** could be beneficial due to the ability of S and O atoms to bind to the undercoordinated Pb<sup>2+</sup> ions and thus heal defects on the surface of the perovskite absorber films.

Another important aspect was the operational stability of the fabricated PSCs. We note that though Mg/Ag electrodes can provide good device efficiency, the operational stability could be compromised by silver diffusion into the ETL and absorber layer. It is known that Al does not easily diffuse into thin films of organic materials, so Al top electrodes were used for stability tests. The devices were exposed to continuous LED illumination providing approximately the same dose of absorbed photons as the standard 100 mW/cm<sup>2</sup> AM1.5G light flux. The equilibrium temperature on the sample surface was 43.5 ± 2.5 °C. All devices

were tested under open circuit conditions, which is known to induce much faster degradation as compared to maximal power point (MPP) tracking or short-circuit operation regimes [44]. All tests were performed under anoxic conditions inside nitrogen glove box, which could be considered as a model of an “ideal encapsulation”. Such approach is fully justified by the fact that our experiments were focused on investigation of intrinsic device stability associated with the behavior of electron transport layer materials, so the contributions from extrinsic stress factors such as oxygen and moisture have to be minimized.

The results of the performed tests are shown in Figure 4, where normalized solar cell parameters are plotted as functions of the aging time. One could notice that while the open circuit voltage remains relatively stable upon aging,  $J_{SC}$  and FF parameters decrease considerably, thus pointing towards a developing problem with the charge extraction and/or transport through ETL to the top electrode.

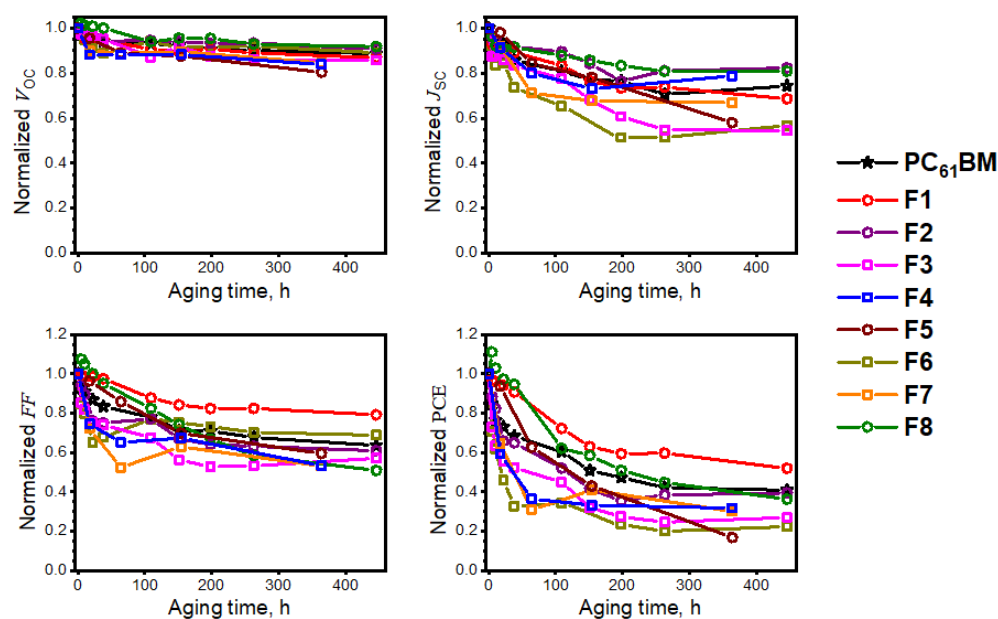


**Figure 4.** The evolution of the normalized device parameters for PSCs assembled with different ETL materials upon aging under continuous exposure to light in open-circuit conditions.

With respect to the correlations between the molecular structures of the investigated fullerene derivatives and operational stability of the corresponding PSCs, we could notice the following. First, the fullerene derivative **F4** with fluoroalkyl side chain could not provide stable device operation. Indeed, moisture-repelling properties of fluorine-containing fullerene derivatives could suppress ambient degradation, whereas the intrinsic aging pathways could be even facilitated due to the decreased adhesion of hydrophobic fluorine-loaded ETL to the highly polar perovskite surface. Among the [70]fullerene derivatives **F2** and **F3**, the former provided somewhat higher stability than the latter presumably due to the presence of longer aliphatic side chain enabling higher material solubility and hence higher uniformity of the coated films, as revealed by IR s-SNOM nanoscale mapping (Figures 2 and S20). The fullerene derivatives with reduced electron affinity **F5–F7** failed to improve the operational stability of PSCs in comparison with the reference devices assembled using standard  $PC_{61}BM$ . On the contrary, the degradation of the cells assembled with the fullerene derivative **F8** was considerably slower than for the reference devices, especially at the initial 100–200 h of aging. The most stable PSCs were fabricated using fullerene derivative **F1**: indeed, only these devices maintained >50% of the initial efficiency after 450 h of continuous light soaking. Thus, fullerene derivative **F1** enables both the highest power conversion efficiency and the best operational stability of PSCs among all the studied fullerene-based ETLs including  $PC_{61}BM$ .

### 3. Discussion

The presented systematic study of a series of fullerene derivatives clearly showed that the structure of the organic addends attached to the fullerene cage and, most importantly, physicochemical properties of the compounds (e.g., solubility, ability to form uniform films, etc.) significantly influence photovoltaic characteristics of PSCs and their operational stability. For example, compound **F4** with fluoroalkyl group and compounds **F6–F7** with two aromatic substituents in cyclopropane ring attached to the fullerene cage are the least soluble in organic solvents, so they produce non-uniform films (fullerene derivative start to crystallize during coating) leading to poor operational stability of the devices. This hypothesis is well-supported by IR *s*-SNOM nanoscale mapping results presented in Figure 2). Fullerene derivative **F8** has oligoether substituent, which enables high solubility and good film formation properties, which result in decent operational stability of PSCs comparable to the reference cells assembled with PC<sub>61</sub>BM.

In this work we have identified compound **F1** as the most promising electron transport material among the studied fullerene derivatives since it outperforms the commonly used PC<sub>61</sub>BM in terms of both device efficiency and stability. We believe that the superior performance of **F1** is associated with its high solubility enabling the formation of highly uniform ETL films and the presence of thiophene ring capable of defect healing at the interface with the perovskite absorber. These findings suggest that performing multiparametric optimization of the molecular structures of the fullerene derivatives could pave a way to the development of a new generation of fullerene-based ETL materials enabling long lifetimes of p-i-n PSCs.

At the current stage, however, the intrinsic stability of PSCs assembled using **F1** as ETL is lagging behind the industrial benchmarks required for practical implementation of perovskite PV technology. Therefore, future efforts should be focused on further modification of **F1** to produce very compact fullerene ETL films completely blocking the perovskite degradation products and thus delivering the desired PSCs operational stability.

### 4. Materials and Methods

#### 4.1. General

Fullerenes C<sub>60</sub> and C<sub>70</sub> were purchased from Neotech Product Ltd. (Saint Petersburg, Russia). All solvents and reagents were procured from Sigma-Aldrich or Acros Organics and used as received if not stated otherwise. Perovskite precursor materials (FAI, PbI<sub>2</sub>), PC<sub>61</sub>BM and PTAA were purchased from FOMaterials Ltd., Chernogolovka, Russia.

The HPLC profiles were obtained using Shimadzu LC20 instrument. The MALDI ToF mass spectra were recorded with Shimadzu Axima Confidence time-of-flight spectrometer (Shimadzu Biotech, Kyoto, Japan) in the reflectron high resolution mode with a nitrogen laser ( $\lambda = 337$  nm). Negative ions were registered. The mass range between 200 and 2000 was scanned. Pyrene was used as a matrix. The NMR spectra were recorded using Bruker Avance 500 MHz (<sup>1</sup>H) spectrometer using the residual solvent signals as a reference. The IR *s*-SNOM measurements were performed as described previously [45].

#### 4.2. Synthesis of **F1–F7**

The synthesis was based on the method developed by Hummelen and Wudl [38]. The corresponding tosylhydrazone (1.3 eq.) was dissolved under an inert atmosphere in 5 mL of dry pyridine in a dried three-necked round-bottom flask equipped with a thermometer and a magnetic stirrer. Then, CH<sub>3</sub>ONa (1.3 eq.) was added, and the mixture was stirred for 15 minutes. A solution of fullerene C<sub>60</sub> or C<sub>70</sub> (500–1000 mg, 1.0 eq.) in 100 mL of 1,2-DCB was added and the reaction mixture was stirred at 70–90 °C for 7 hours. The progress of the reaction was monitored by HPLC. When the reaction was complete (no further fullerene conversion is observed), the system was cooled down to the room temperature, the solids were separated by filtration, the filtrate was concentrated to dryness at the rotary evaporator. The residue was purified by column chromatography on silica gel using as eluents the mixtures of hexanes and carbon disulfide or a mixture of petroleum ether and toluene

in volume ratios varied from 4:1 to 1:1. The isolated monoaddition products (mixtures of methanofullerenes and fulleroids) were then redissolved in 1,2-DCB (concentration of 3–5 mg mL<sup>-1</sup>) and the resulting solutions were heated at reflux for ca. 8 h to accomplish the transition of fulleroids to methanofullerene. Then, the solutions were cooled down and the purity of the products was checked by HPLC. Additional purification by column chromatography was performed if necessary to remove trace amounts of C<sub>60</sub> (or C<sub>70</sub>) and bisfunctionalization products. The solutions of the target fullerene derivatives were concentrated to the minimal volumes prior crystallization is observed and 3-fold volume amount of isopropanol was slowly added under gentle stirring to induce precipitation of the fullerene derivatives. The precipitates were collected by decantation, washed with isopropanol, acetone and dried in vacuum.

**F1.** Yield: 28%. <sup>1</sup>H NMR (500 MHz, Chloroform-*d*, *J*, Hz,  $\delta$ , ppm): 7.48–7.46 (m, 2H), 7.13 (dd, *J* = 5.1, 3.6 Hz, 1H), 3.67 (s, 3H), 2.94–2.89 (m, 2H), 2.43 (t, *J* = 7.2 Hz, 2H), 1.97–1.85 (m, 2H). <sup>13</sup>C NMR (126 MHz, CDCl<sub>3</sub>,  $\delta$ , ppm): 174.01, 148.54, 147.77, 145.83, 145.40, 145.37, 145.35, 145.28, 145.27, 144.97, 144.90, 144.83, 144.74, 144.64, 144.31, 143.96, 143.95, 143.28, 143.19, 143.16, 143.10, 143.07, 142.36, 142.35, 142.28, 142.26, 141.12, 140.87, 139.56, 138.30, 138.28, 132.01, 126.26, 80.23, 77.41, 77.36, 77.16, 76.91, 51.76, 46.22, 34.39, 34.11, 26.75, 24.89. MALDI ToF MS (*m/z*): 894.33 [M]<sup>-</sup>.

**F2** Yield (two isomers): 25%. <sup>1</sup>H NMR (500 MHz, Chloroform-*d*, *J*, Hz,  $\delta$ , ppm): 7.91 (s, 2H), 7.61–7.47 (m, 2H), 7.46–7.37 (m, 1H), 4.06 (t, *J* = 6.8 Hz, 2H), 2.52–2.39 (m, 4H), 2.24–1.97 (m, 4H), 1.83–1.42 (m, 2H), 1.41–1.19 (m, 6H), 0.94–0.82 (m, 3H). <sup>13</sup>C NMR (126 MHz, CDCl<sub>3</sub>,  $\delta$ , ppm): 173.24, 172.99, 156.13, 155.42, 153.34, 152.30, 152.08, 151.63, 151.56, 151.35, 151.34, 151.28, 151.03, 150.99, 150.74, 150.68, 150.13, 150.05, 149.91, 149.81, 149.58, 149.53, 149.47, 149.35, 149.33, 149.32, 149.28, 149.26, 148.99, 148.78, 148.72, 148.71, 148.68, 148.66, 148.63, 148.57, 148.56, 148.46, 148.44, 148.38, 148.35, 148.22, 148.17, 148.12, 148.06, 147.72, 147.68, 147.58, 147.52, 147.34, 147.31, 147.23, 147.21, 147.18, 147.14, 147.01, 146.98, 146.94, 146.92, 146.71, 146.49, 146.44, 146.24, 146.07, 146.01, 145.97, 145.80, 145.64, 145.61, 145.45, 145.03, 145.02, 144.92, 144.67, 144.59, 144.33, 144.27, 144.24, 144.07, 144.02, 143.89, 143.78, 143.66, 143.47, 143.39, 143.25, 143.18, 143.10, 142.79, 142.72, 142.65, 142.64, 141.94, 141.90, 141.88, 141.75, 141.65, 141.57, 141.47, 141.09, 140.30, 139.85, 139.43, 139.06, 138.22, 138.07, 137.46, 134.15, 133.99, 132.98, 132.96, 132.63, 132.36, 132.34, 132.33, 131.98, 131.83, 131.76, 131.66, 131.42, 131.37, 131.33, 131.05, 130.91, 130.89, 130.80, 130.57, 128.70, 128.68, 128.35, 77.42, 77.16, 76.91, 72.04, 69.96, 64.96, 36.06, 34.25, 34.22, 31.89, 29.10, 28.80, 26.06, 22.76, 21.89, 14.27. MALDI ToF MS (*m/z*): 1114.37 [M]<sup>-</sup>.

**F3.** Yield (two isomers): 23%. <sup>1</sup>H NMR (500 MHz, Chloroform-*d*, *J*, Hz,  $\delta$ , ppm): 7.92 (s, 2H), 7.56–7.50 (m, 2H), 7.47–7.42 (m, 1H), 4.07 (t, *J* = 6.8 Hz, 2H), 2.87–2.72 (m, 4H), 1.68–1.59 (m, 2H), 1.40–1.19 (m, 10H), 0.90–0.85 (m, 3H). <sup>13</sup>C NMR (126 MHz, CDCl<sub>3</sub>,  $\delta$ , ppm): 172.61, 156.07, 155.37, 152.27, 152.05, 151.63, 151.35, 151.29, 151.03, 151.00, 150.73, 150.68, 149.59, 149.53, 149.35, 149.33, 149.29, 148.74, 148.70, 148.67, 148.59, 148.56, 148.48, 148.20, 148.11, 148.02, 147.71, 147.67, 147.58, 147.51, 147.17, 147.02, 146.45, 146.23, 146.06, 145.99, 145.83, 145.81, 144.72, 144.68, 144.21, 144.07, 144.05, 143.89, 143.80, 143.50, 143.43, 142.82, 142.69, 141.99, 141.75, 141.54, 141.15, 140.45, 139.51, 138.95, 136.91, 134.13, 133.98, 132.99, 132.97, 131.82, 131.07, 130.92, 130.90, 130.83, 130.60, 128.79, 128.54, 128.38, 125.45, 71.95, 69.91, 65.26, 35.21, 31.89, 31.40, 29.10, 28.74, 26.10, 22.76, 14.26. MALDI ToF MS (*m/z*): 1100.43 [M]<sup>-</sup>.

**F4.** Yield: 27%. <sup>1</sup>H NMR (500 MHz, Chloroform-*d*, *J*, Hz,  $\delta$ , ppm): 7.95–7.92 (m, 2H), 7.59–7.55 (m, 2H), 7.52–7.48 (m, 1H), 6.05 (tt, *J* = 51.9, 5.4 Hz, 1H), 4.57 (t, *J* = 13.9 Hz, 2H), 3.31–3.21 (m, 2H), 3.01–2.92 (m, 2H). <sup>13</sup>C NMR (126 MHz, CDCl<sub>3</sub>,  $\delta$ , ppm): 171.08, 148.56, 147.28, 145.88, 145.38, 145.37, 145.24, 145.11, 144.98, 144.90, 144.87, 144.80, 144.72, 144.66, 144.24, 143.92, 143.31, 143.24, 143.20, 143.17, 143.13, 142.40, 142.29, 141.23, 140.96, 138.34, 137.81, 136.05, 132.25, 128.84, 128.76, 79.52, 77.41, 50.58, 31.45, 29.47. <sup>19</sup>F NMR (471 MHz, Chloroform-*d*, *J*, Hz,  $\delta$ , ppm): –119.39––119.77 (m), –125.15 (t, *J* = 8.7 Hz), –129.58––129.97 (m), –136.72––137.56 (m). MALDI ToF MS (*m/z*): 1096.27 [M]<sup>-</sup>.

**F5.** Yield: 23%.  $^1\text{H}$  NMR (500 MHz, Chloroform-*d*, *J*, Hz,  $\delta$ , ppm): 7.71 (d, *J* = 8.3 Hz, 1H), 6.65–6.59 (m, 2H), 4.21–4.07 (m, 2H), 4.07–4.02 (m, 2H), 3.69 (s, 3H), 3.63 (s, 3H), 2.46 (s, 3H), 2.45–2.43 (m, 2H), 2.37 (t, *J* = 7.0 Hz, 2H), 2.06–1.82 (m, 8H).  $^{13}\text{C}$  NMR (126 MHz,  $\text{CDCl}_3$ ,  $\delta$ , ppm): 174.04, 173.83, 160.33, 158.37, 150.49, 149.81, 148.89, 148.74, 146.32, 146.21, 145.73, 145.29, 145.20, 145.15, 145.09, 144.98, 144.95, 144.88, 144.83, 144.77, 144.58, 144.47, 144.38, 144.10, 144.01, 143.95, 143.95, 143.91, 143.85, 143.20, 143.16, 143.11, 143.09, 143.07, 143.03, 142.64, 142.54, 142.33, 142.29, 142.27, 142.21, 141.20, 141.00, 140.95, 140.68, 138.31, 138.11, 138.06, 136.51, 133.39, 119.05, 104.76, 100.17, 82.39, 79.77, 67.64, 67.42, 51.75, 43.67, 33.86, 33.80, 29.85, 29.29, 28.90, 21.98, 21.85, 20.07. MALDI ToF MS (*m/z*): 1084.47 [ $\text{M}$ ] $^-$ .

**F6.** Yield: 21%.  $^1\text{H}$  NMR (500 MHz, Chloroform-*d*, *J*, Hz,  $\delta$ , ppm): 8.21–8.15 (m, 2H), 7.72 (d, *J* = 8.6 Hz, 1H), 7.48 (t, *J* = 7.7 Hz, 2H), 7.41–7.35 (m, 1H), 6.75 (d, *J* = 8.6 Hz, 1H), 4.22–4.17 (m, 3H), 3.88 (s, 3H), 3.92–3.83 (m, 2H), 1.71–1.59 (m, 1H), 1.53–1.23 (m, 8H), 0.94–0.86 (m, 6H).  $^{13}\text{C}$  NMR (126 MHz,  $\text{CDCl}_3$ ,  $\delta$ , ppm): 154.39, 152.95, 152.94, 150.14, 149.33, 149.26, 148.89, 145.98, 145.82, 145.75, 145.37, 145.33, 145.30, 145.25, 145.20, 145.17, 144.86, 144.82, 144.80, 144.78, 144.36, 144.34, 144.31, 144.28, 144.10, 144.07, 143.99, 143.91, 143.12, 143.10, 143.08, 143.04, 143.01, 142.98, 142.63, 142.53, 142.43, 142.31, 142.29, 142.25, 142.13, 141.47, 141.46, 141.03, 140.92, 140.76, 138.78, 138.77, 138.38, 138.27, 136.93, 131.81, 128.43, 127.95, 126.98, 126.97, 123.76, 123.74, 106.49, 79.56, 78.52, 76.09, 76.03, 61.76, 61.73, 55.98, 54.29, 40.48, 40.45, 30.43, 30.41, 29.19, 29.18, 23.85, 23.68, 23.28, 23.25, 14.34, 14.32, 11.29, 11.09. MALDI ToF MS (*m/z*): 1074.65 [ $\text{M}$ ] $^-$ .

**F7.** Yield: 20%.  $^1\text{H}$  NMR (500 MHz, Chloroform-*d*, *J*, Hz,  $\delta$ , ppm): 7.67 (d, *J* = 8.6 Hz, 1H), 7.65 (dd, *J* = 3.6, 1.2 Hz, 1H), 7.36 (dd, *J* = 5.2, 1.2 Hz, 1H), 7.06 (dd, *J* = 5.2, 3.6 Hz, 1H), 6.76 (d, *J* = 8.6 Hz, 1H), 4.22–4.21 (m, 3H), 3.95–3.83 (m, 2H), 3.9 (s, 3H), 1.71–1.60 (m, 1H), 1.54–1.23 (m, 8H), 0.93–0.87 (m, 6H).  $^{13}\text{C}$  NMR (126 MHz,  $\text{CDCl}_3$ ,  $\delta$ , ppm): 154.58, 154.57, 153.96, 152.82, 152.80, 149.95, 148.96, 148.81, 148.56, 145.90, 145.80, 145.80, 145.69, 145.40, 145.37, 145.35, 145.32, 145.31, 145.29, 145.25, 144.89, 144.82, 144.51, 144.50, 144.45, 144.36, 144.15, 144.12, 144.03, 143.98, 143.11, 143.06, 143.04, 143.02, 142.58, 142.56, 142.47, 142.39, 142.38, 142.31, 142.30, 142.27, 142.14, 141.52, 141.42, 141.41, 141.00, 140.94, 140.74, 138.93, 138.83, 138.53, 137.00, 130.82, 126.95, 126.93, 126.14, 126.01, 123.48, 123.47, 80.00, 78.33, 76.18, 76.11, 61.80, 61.78, 56.00, 48.02, 40.49, 40.47, 30.44, 30.42, 29.85, 29.20, 23.86, 23.69, 23.26, 14.34, 14.32, 11.28, 11.09. MALDI ToF MS (*m/z*): 1082.84 [ $\text{M}$ ] $^-$ .

#### 4.3. Synthesis of **F8**

The synthesis was based on the method reported previously [39]. Briefly, 1.5 eq. of the sulfonium salt and equimolar amount of sodium hydride (60% in paraffin oil) were placed into dried 100 mL three-neck round-bottom flask filled with argon. Afterwards, 5 mL of vigorously dried toluene was added to dissolve the paraffin oil followed by 45 mL of anhydrous THF. The reaction mixture was stirred at room temperature for 1 h and the reaction was accompanied by partial NaBr precipitation. Afterwards, the prepared solution of the ylide was poured in a stream of argon into a dropping funnel connected to a 500 mL three-neck round-bottom flask loaded with 300 mL of fullerene solution in vigorously dried toluene (concentration 2.0 mg mL $^{-1}$ ). The ylide solution was added dropwise to the fullerene solution under intense stirring within the period of 30–40 min. Afterwards, the fullerene conversion was checked by thin-layer chromatography and an additional portion of ylide was added if the conversion was below 60%. The reaction mixture was filtered and the filtrate was concentrated to dryness at the rotary evaporator. The residue was redissolved in toluene, diluted with two volumes of hexanes and the resulting solution was processed by column chromatography on silica using toluene-hexanes mixtures as eluent. The target compound **F8** was eluted after unreacted C<sub>60</sub>, the solution concentrated to dryness, the residue was washed with diethyl ether and hexanes and dried in a vacuum.

**F8.** Yield: 35%.  $^1\text{H}$  NMR (500 MHz, Chloroform-*d*, *J*, Hz,  $\delta$ , ppm): 4.84 (s, 1H), 4.65–4.59 (m, 2H), 3.99–3.89 (m, 2H), 3.80–3.72 (m, 2H), 3.70–3.64 (m, 2H), 3.57 (q, *J* = 7.0 Hz, 2H), 1.25 (t, *J* = 7.0 Hz, 3H).  $^{13}\text{C}$  NMR (126 MHz,  $\text{CDCl}_3$ ,  $\delta$ , ppm): 166.56, 148.39, 145.82, 145.74, 145.42, 145.37, 145.34, 145.24, 145.22, 144.87, 144.84, 144.82, 144.76, 144.74, 144.58, 144.12,

143.89, 143.43, 143.24, 143.16, 143.12, 143.11, 142.96, 142.59, 142.36, 142.25, 142.22, 141.30, 141.08, 140.78, 136.55, 70.99, 70.67, 70.01, 69.18, 66.95, 65.49, 38.99, 15.37. MALDI ToF MS ( $m/z$ ): 894.33 [M]<sup>-</sup>.

#### 4.4. PSCs Fabrication and Characterization

Glass/ITO substrates (Kintec, 15  $\Omega$ /sq.) were sequentially cleaned with distilled water, acetone, and isopropanol. Afterwards, the dried substrates were subjected to the air plasma treatment for 5 min. PTAA was spin coated from a chlorobenzene solution (2.5 mg mL<sup>-1</sup>) at 4000 rpm for 30 s and annealed at 125 °C for 15 min in a nitrogen atmosphere. The Cs<sub>0.12</sub>FA<sub>0.88</sub>PbI<sub>3</sub> precursor solution was prepared by dissolving CsI (0.2434 g), FAI (1.1806 g), and PbI<sub>2</sub> (3.5958 g) in a mixture of 1.2 mL of anhydrous DMSO and 4.8 mL of anhydrous N,N-dimethylacetamide. The resulting solution was filtered through a 0.45  $\mu$ m PTFE syringe filter prior spin-coating.

The perovskite precursor solution (100  $\mu$ L) was spun at 4000 rpm and quenched after 36 s with 105  $\mu$ L of chlorobenzene. Afterwards, the films were annealed at 105 °C for 5 min. The PC<sub>61</sub>BM was deposited from a chlorobenzene solution (30 mg mL<sup>-1</sup>) at 3000 rpm for 20 s. The fullerene derivatives F1–F8 were deposited from chlorobenzene solutions (20.2, 16.2, 30, 30, 17.2, 30, 30, and 18.8 mg mL<sup>-1</sup>, respectively) at the spinning frequencies of 1000–3000 rpm for 20 s. The solar cells were completed by the thermal evaporation of Mg (30 nm)/Ag (110 nm) or Al (120 nm, for stability tests) contacts. The device area was ca. 0.075 cm<sup>2</sup>.

The current-voltage characteristics of the solar cells were measured in an inert nitrogen atmosphere inside a glove box using the simulated AM1.5G illumination (100 mW/cm<sup>2</sup>) provided by a K. H. Steuernagel Lichttechnik GmbH solar simulator and a shadow mask with the aperture of 0.07 cm<sup>2</sup>. The intensity of the illumination was checked before each measurement using a calibrated silicon diode with a known spectral response. The J–V curves were recorded using Advantest 6240A source-measurement units in forward and reverse directions with the scan rate of 10 mV s<sup>-1</sup> at the temperature of 25 °C. The EQE spectra were measured under anoxic nitrogen atmosphere using a LOMO (Russia) instrument equipped with 150 W xenon lamp as a light source for generation of monochromatic illumination for the measured cells with the step of 5 nm.

The aging experiments were performed using continuous LED illumination providing approximately the same dose of absorbed photons as the standard 100 mW/cm<sup>2</sup> AM1.5G light flux. The equilibrium temperature on the sample surface was 43.5  $\pm$  2.5 °C. All devices were tested under open circuit conditions, which is known to induce much faster degradation as compared to maximal power point (MPP) tracking or short-circuit operation regimes. All tests were performed under anoxic conditions inside nitrogen glove box, which could be considered as a model of an “ideal encapsulation”.

**Supplementary Materials:** The following supporting information can be downloaded at: <https://www.mdpi.com/article/10.3390/inorganics11040153/s1>, Figure S1: HPLC traces of compounds F1–F8; Figure S2: MALDI ToF mass spectra of compounds F1–F8; Figures S3–S18: <sup>1</sup>H, <sup>13</sup>C and 2D NMR spectra of compounds F1–F8; Figure S19: PL data for perovskite/ETL stacks; Figure S20: IR s-SNOM data for perovskite/ETL stacks; Figure S21: Dependence of the perovskite solar cell parameters on the deposition rate of the fullerene derivative F1 (20.2 mg mL<sup>-1</sup> solution in chlorobenzene) used to form electron transport layer in the devices.

**Author Contributions:** Conceptualization, P.A.T. and S.M.A.; methodology, P.A.T.; investigation, V.V.O., A.V.M., A.E.G., E.A.K. and A.S.P.; writing—original draft preparation, V.V.O.; writing—review and editing, P.A.T.; supervision, P.A.T.; project administration, P.A.T.; funding acquisition, S.M.A. All authors have read and agreed to the published version of the manuscript.

**Funding:** This research was funded by the Ministry of Science and Higher Education of the Russian Federation (Grant No. 075-15-2022-1216).

**Data Availability Statement:** The data presented in this study are available in the article and supplementary material.

**Conflicts of Interest:** The authors declare no conflict of interest.

## References

1. Green, M.A.; Dunlop, E.D.; Hohl-Ebinger, J.; Yoshita, M.; Kopidakis, N.; Bothe, K.; Hinken, D.; Rauer, M.; Hao, X. Solar Cell Efficiency Tables (Version 60). *Prog. Photovolt.* **2022**, *30*, 687–701. [[CrossRef](#)]
2. Sahare, S.; Pham, H.D.; Angmo, D.; Ghoderao, P.; MacLeod, J.; Khan, S.B.; Lee, S.; Singh, S.P.; Sonar, P. Emerging Perovskite Solar Cell Technology: Remedial Actions for the Foremost Challenges. *Adv. Energy Mater.* **2021**, *11*, 2101085. [[CrossRef](#)]
3. Kim, J.Y.; Lee, J.-W.; Jung, H.S.; Shin, H.; Park, N.-G. High-Efficiency Perovskite Solar Cells. *Chem. Rev.* **2020**, *120*, 7867–7918. [[CrossRef](#)]
4. Schulz, P.; Cahen, D.; Kahn, A. Halide Perovskites: Is It All about the Interfaces? *Chem. Rev.* **2019**, *119*, 3349–3417. [[CrossRef](#)] [[PubMed](#)]
5. Akbulatov, A.F.; Frolova, L.A.; Griffin, M.P.; Gearba, I.R.; Dolocan, A.; Vanden Bout, D.A.; Tsarev, S.; Katz, E.A.; Shestakov, A.F.; Stevenson, K.J.; et al. Effect of Electron-Transport Material on Light-Induced Degradation of Inverted Planar Junction Perovskite Solar Cells. *Adv. Energy Mater.* **2017**, *7*, 1700476. [[CrossRef](#)]
6. Wu, S.; Chen, R.; Zhang, S.; Babu, B.H.; Yue, Y.; Zhu, H.; Yang, Z.; Chen, C.; Chen, W.; Huang, Y.; et al. A Chemically Inert Bismuth Interlayer Enhances Long-Term Stability of Inverted Perovskite Solar Cells. *Nat. Commun.* **2019**, *10*, 1161. [[CrossRef](#)]
7. Chen, R.; Zhang, W.; Guan, X.; Raza, H.; Zhang, S.; Zhang, Y.; Troshin, P.A.; Kuklin, S.A.; Liu, Z.; Chen, W. Rear Electrode Materials for Perovskite Solar Cells. *Adv. Funct. Mater.* **2022**, *32*, 2200651. [[CrossRef](#)]
8. Elnaggar, M.; Boldyreva, A.G.; Elshobaki, M.; Tsarev, S.A.; Fedotov, Y.S.; Yamilova, O.R.; Bredikhin, S.I.; Stevenson, K.J.; Aldoshin, S.M.; Troshin, P.A. Decoupling Contributions of Charge-Transport Interlayers to Light-Induced Degradation of P-i-n Perovskite Solar Cells. *Sol. RRL* **2020**, *4*, 2000191. [[CrossRef](#)]
9. Liu, K.; Tian, C.; Liang, Y.; Luo, Y.; Xie, L.; Wei, Z. Progress toward Understanding the Fullerene-Related Chemical Interactions in Perovskite Solar Cells. *Nano Res.* **2022**, *15*, 7139–7153. [[CrossRef](#)]
10. Zahran, R.; Hawash, Z. Fullerene-Based Inverted Perovskite Solar Cell: A Key to Achieve Promising, Stable, and Efficient Photovoltaics. *Adv. Mater. Inter.* **2022**, *9*, 2201438. [[CrossRef](#)]
11. Deng, L.-L.; Xie, S.-Y.; Gao, F. Fullerene-Based Materials for Photovoltaic Applications: Toward Efficient, Hysteresis-Free, and Stable Perovskite Solar Cells. *Adv. Electron. Mater.* **2018**, *4*, 1700435. [[CrossRef](#)]
12. Foo, S.; Thambidurai, M.; Senthil Kumar, P.; Yuvakkumar, R.; Huang, Y.; Dang, C. Recent Review on Electron Transport Layers in Perovskite Solar Cells. *Int. J. Energy Res.* **2022**, *46*, 21441–21451. [[CrossRef](#)]
13. Kim, T.; Lim, J.; Song, S. Recent Progress and Challenges of Electron Transport Layers in Organic–Inorganic Perovskite Solar Cells. *Energies* **2020**, *13*, 5572. [[CrossRef](#)]
14. Zhang, K.; Yu, H.; Liu, X.; Dong, Q.; Wang, Z.; Wang, Y.; Chen, N.; Zhou, Y.; Song, B. Fullerenes and Derivatives as Electron Transport Materials in Perovskite Solar Cells. *Sci. China Chem.* **2017**, *60*, 144–150. [[CrossRef](#)]
15. Yao, Y.; Cheng, C.; Zhang, C.; Hu, H.; Wang, K.; De Wolf, S. Organic Hole-Transport Layers for Efficient, Stable, and Scalable Inverted Perovskite Solar Cells. *Adv. Mater.* **2022**, *34*, 2203794. [[CrossRef](#)]
16. Sun, X.; Zhu, Z.; Li, Z. Recent Advances in Developing High-Performance Organic Hole Transporting Materials for Inverted Perovskite Solar Cells. *Front. Optoelectron.* **2022**, *15*, 46. [[CrossRef](#)]
17. Ahmad, T.; Wilk, B.; Radicchi, E.; Fuentes Pineda, R.; Spinelli, P.; Herterich, J.; Castriotta, L.A.; Dasgupta, S.; Mosconi, E.; De Angelis, F.; et al. New Fullerene Derivative as an N-Type Material for Highly Efficient, Flexible Perovskite Solar Cells of a P-i-n Configuration. *Adv. Funct. Mater.* **2020**, *30*, 2004357. [[CrossRef](#)]
18. Tian, C.; Betancourt-Solis, G.; Nan, Z.; Liu, K.; Lin, K.; Lu, J.; Xie, L.; Echegoyen, L.; Wei, Z. Efficient and Stable Inverted Perovskite Solar Cells Enabled by Inhibition of Self-Aggregation of Fullerene Electron-Transporting Compounds. *Sci. Bull.* **2021**, *66*, 339–346. [[CrossRef](#)] [[PubMed](#)]
19. Fernandez-Delgado, O.; Chandrasekhar, P.S.; Cano-Sampaio, N.; Simon, Z.C.; Puente-Santiago, A.R.; Liu, F.; Castro, E.; Echegoyen, L. The Role of Fullerene Derivatives in Perovskite Solar Cells: Electron Transporting or Electron Extraction Layers? *J. Mater. Chem. C* **2021**, *9*, 10759–10767. [[CrossRef](#)]
20. Elnaggar, M.; Elshobaki, M.; Mumyatov, A.; Luchkin, S.Y.; Dremova, N.N.; Stevenson, K.J.; Troshin, P.A. Molecular Engineering of the Fullerene-Based Electron Transport Layer Materials for Improving Ambient Stability of Perovskite Solar Cells. *Sol. RRL* **2019**, *3*, 1900223. [[CrossRef](#)]
21. Chen, R.; Wang, W.; Bu, T.; Ku, Z.; Zhong, J.; Peng, Y.; Xiao, S.; You, W.; Huang, F.; Cheng, Y.; et al. Low-Cost Fullerene Derivative as an Efficient Electron Transport Layer for Planar Perovskite Solar Cells. *Acta Phys.-Chim. Sinica* **2019**, *35*, 401–407. [[CrossRef](#)]
22. Liu, F.; Xing, Z.; Ren, Y.; Huang, R.-J.; Xu, P.-Y.; Xie, F.-F.; Li, S.-H.; Zhong, X. Tailoring Functional Terminals on Solution-Processable Fullerene Electron Transporting Materials for High Performance Perovskite Solar Cells. *Nanomaterials* **2022**, *12*, 1046. [[CrossRef](#)] [[PubMed](#)]
23. Pascual, J.; Collavini, S.; Völker, S.F.; Phung, N.; Palacios-Lidon, E.; Irusta, L.; Grande, H.-J.; Abate, A.; Tena-Zaera, R.; Delgado, J.L. Unravelling Fullerene–Perovskite Interactions Introduces Advanced Blend Films for Performance-Improved Solar Cells. *Sust. Energy Fuels* **2019**, *3*, 2779–2787. [[CrossRef](#)]
24. Shao, G.; Niu, C.; Liu, H.-W.; Yang, H.; Chen, J.-S.; Yao, Y.-R.; Yang, S.; Wang, G.-W. [60]Fullerene-Fused Cyclopentanes: Mechanosynthesis and Photovoltaic Application. *Org. Lett.* **2023**, *25*, 1229–1234. [[CrossRef](#)] [[PubMed](#)]

25. Przypis, L.; Ahmad, T.; Misztal, K.; Honisz, D.; Radicchi, E.; Mosconi, E.; Domagala, W.; De Angelis, F.; Wojciechowski, K. Designing New Indene-Fullerene Derivatives as Electron-Transporting Materials for Flexible Perovskite Solar Cells. *J. Phys. Chem. C* **2021**, *125*, 27344–27353. [[CrossRef](#)]
26. Younes, E.M.; Gurung, A.; Bahrami, B.; El-Maghraby, E.M.; Qiao, Q. Enhancing Efficiency and Stability of Inverted Structure Perovskite Solar Cells with Fullerene C<sub>60</sub> Doped PC<sub>61</sub>BM Electron Transport Layer. *Carbon* **2021**, *180*, 226–236. [[CrossRef](#)]
27. Li, S.-H.; Xing, Z.; Wu, B.-S.; Chen, Z.-C.; Yao, Y.-R.; Tian, H.-R.; Li, M.-F.; Yun, D.-Q.; Deng, L.-L.; Xie, S.-Y.; et al. Hybrid Fullerene-Based Electron Transport Layers Improving the Thermal Stability of Perovskite Solar Cells. *ACS Appl. Mater. Interfaces* **2020**, *12*, 20733–20740. [[CrossRef](#)]
28. Liu, Z.; Siekmann, J.; Klingebiel, B.; Rau, U.; Kirchartz, T. Interface Optimization via Fullerene Blends Enables Open-Circuit Voltages of 1.35 V in CH<sub>3</sub>NH<sub>3</sub>Pb(I<sub>0.8</sub>Br<sub>0.2</sub>)<sub>3</sub> Solar Cells. *Adv. Energy Mater.* **2021**, *11*, 2003386. [[CrossRef](#)]
29. Saranin, D.; Pescetelli, S.; Pazniak, A.; Rossi, D.; Liedl, A.; Yakusheva, A.; Luchnikov, L.; Podgorny, D.; Gostishev, P.; Didenko, S.; et al. Transition Metal Carbides (MXenes) for Efficient NiO-Based Inverted Perovskite Solar Cells. *Nano Energy* **2021**, *82*, 105771. [[CrossRef](#)]
30. Luo, Z.; Wu, F.; Zhang, T.; Zeng, X.; Xiao, Y.; Liu, T.; Zhong, C.; Lu, X.; Zhu, L.; Yang, S.; et al. Designing a Perylene Diimide/Fullerene Hybrid as Effective Electron Transporting Material in Inverted Perovskite Solar Cells with Enhanced Efficiency and Stability. *Angew. Chem. Int. Ed.* **2019**, *58*, 8520–8525. [[CrossRef](#)]
31. Cheng, Z.; Fang, Y.; Wang, A.; Ma, T.; Liu, F.; Gao, S.; Yan, S.; Di, Y.; Qin, T. Highly Soluble Dendritic Fullerene Derivatives as Electron Transport Material for Perovskite Solar Cells. *J. Cent. South Univ.* **2021**, *28*, 3714–3727. [[CrossRef](#)]
32. Huang, H.-H.; Tsai, H.; Raja, R.; Lin, S.-L.; Ghosh, D.; Hou, C.-H.; Shyue, J.-J.; Tretiak, S.; Chen, W.; Lin, K.-F.; et al. Robust Unencapsulated Perovskite Solar Cells Protected by a Fluorinated Fullerene Electron Transporting Layer. *ACS Energy Lett.* **2021**, *6*, 3376–3385. [[CrossRef](#)]
33. Jia, L.; Zhang, L.; Ding, L.; Yang, S. Using Fluorinated and Crosslinkable Fullerene Derivatives to Improve the Stability of Perovskite Solar Cells. *J. Semicond.* **2021**, *42*, 120201. [[CrossRef](#)]
34. Xing, Z.; Li, S.-H.; Xie, F.-F.; Xu, P.-Y.; Deng, L.-L.; Zhong, X.; Xie, S.-Y. Mixed Fullerene Electron Transport Layers with Fluorocarbon Chains Assembling on the Surface: A Moisture-Resistant Coverage for Perovskite Solar Cells. *ACS Appl. Mater. Interfaces* **2020**, *12*, 35081–35087. [[CrossRef](#)] [[PubMed](#)]
35. Troshin, P.A.; Khakina, E.A.; Egginger, M.; Goryachev, A.E.; Troyanov, S.I.; Fuchsbaauer, A.; Peregodov, A.S.; Lyubovskaya, R.N.; Razumov, V.F.; Sariciftci, N.S. Self-Assembly of Thiophene- and Furan-Appended Methanofullerenes with Poly(3-Hexylthiophene) in Organic Solar Cells. *ChemSusChem* **2010**, *3*, 356–366. [[CrossRef](#)] [[PubMed](#)]
36. Mumyatov, A.V.; Goryachev, A.E.; Prudnov, F.A.; Mukhacheva, O.A.; Sagdullina, D.K.; Chernyak, A.V.; Troyanov, S.I.; Troshin, P.A. Monocyclopropanated Fullerene Derivatives with Decreased Electron Affinity as Promising Electron Acceptor Materials for Organic Solar Cells. *Synth. Met.* **2020**, *270*, 116565. [[CrossRef](#)]
37. Mumyatov, A.V.; Troshin, P.A. A Review on Fullerene Derivatives with Reduced Electron Affinity as Acceptor Materials for Organic Solar Cells. *Energies* **2023**, *16*, 1924. [[CrossRef](#)]
38. Hummelen, J.C.; Knight, B.W.; LePeq, F.; Wudl, F.; Yao, J.; Wilkins, C.L. Preparation and Characterization of Fulleroid and Methanofullerene Derivatives. *J. Org. Chem.* **1995**, *60*, 532–538. [[CrossRef](#)]
39. Wang, Y.; Cao, J.; Schuster, D.I.; Wilson, S.R. A Superior Synthesis of [6,6]-Methanofullerenes: The Reaction of Sulfonium Ylides with C<sub>60</sub>. *Tetrahedron Lett.* **1995**, *36*, 6843–6846. [[CrossRef](#)]
40. Wienk, M.M.; Kroon, J.M.; Verhees, W.J.H.; Knol, J.; Hummelen, J.C.; van Hal, P.A.; Janssen, R.A.J. Efficient Methano[70]Fullerene/MDMO-PPV Bulk Heterojunction Photovoltaic Cells. *Angew. Chem. Int. Ed.* **2003**, *42*, 3371–3375. [[CrossRef](#)]
41. Troshin, P.A.; Peregodov, A.S.; Peregodova, S.M.; Lyubovskaya, R.N. Highly Regio- and Stereoselective [2+3] Cycloadditions of Azomethine Ylides to [70]Fullerene. *Eur. J. Org. Chem.* **2007**, *2007*, 5861–5866. [[CrossRef](#)]
42. Powell, W.H.; Cozzi, F.; Moss, G.P.; Thilgen, C.; Hwu, R.J.-R.; Yerin, A. Nomenclature for the C<sub>60</sub>-Ih and C<sub>70</sub>-D<sub>5h</sub>(6) Fullerenes (IUPAC Recommendations 2002). *Pure Appl. Chem.* **2002**, *74*, 629–695. [[CrossRef](#)]
43. Gharibzadeh, S.; Fassel, P.; Hossain, I.M.; Rohrbeck, P.; Frericks, M.; Schmidt, M.; Duong, T.; Khan, M.R.; Abzieher, T.; Nejand, B.A.; et al. Two Birds with One Stone: Dual Grain-Boundary and Interface Passivation Enables >22% Efficient Inverted Methylammonium-Free Perovskite Solar Cells. *Energy Environ. Sci.* **2021**, *14*, 5875–5893. [[CrossRef](#)]
44. Domanski, K.; Alharbi, E.A.; Hagfeldt, A.; Grätzel, M.; Tress, W. Systematic Investigation of the Impact of Operation Conditions on the Degradation Behaviour of Perovskite Solar Cells. *Nat. Energy* **2018**, *3*, 61–67. [[CrossRef](#)]
45. Emelianov, N.A.; Ozerova, V.V.; Zhidkov, I.S.; Korchagin, D.V.; Shilov, G.V.; Litvinov, A.L.; Kurmaev, E.Z.; Frolova, L.A.; Aldoshin, S.M.; Troshin, P.A. Nanoscale Visualization of Photodegradation Dynamics of MAPbI<sub>3</sub> Perovskite Films. *J. Phys. Chem. Lett.* **2022**, *13*, 2744–2749. [[CrossRef](#)] [[PubMed](#)]

**Disclaimer/Publisher's Note:** The statements, opinions and data contained in all publications are solely those of the individual author(s) and contributor(s) and not of MDPI and/or the editor(s). MDPI and/or the editor(s) disclaim responsibility for any injury to people or property resulting from any ideas, methods, instructions or products referred to in the content.